Materials Research Bulletin 107 (2018) 255–263

Contents lists available at ScienceDirect

Materials Research Bulletin

journal homepage: www.elsevier.com/locate/matresbu

Step-by-step synthesis of iron-oxide nanoparticles attached to graphene oxide: A study on the composite properties and architecture

Pablo Tancredi[a,*], Oscar Moscoso Londoño[b,c], Patricia C. Rivas Rojas[a], Marcelo Knobel[b], Leandro M. Socolovsky[d]

[a] Laboratorio de Sólidos Amorfos, Instituto de Tecnologías y Ciencias de la Ingeniería "Hilario Fernández Long", Facultad de Ingeniería, Universidad de Buenos Aires – CONICET, Buenos Aires, Argentina
[b] Laboratório de Materiais e Baixas Temperaturas, Instituto de Física 'Gleb Wataghin', Universidade Estadual de Campinas, Campinas, Brazil
[c] Universidad Autónoma de Manizales, Antigua Estación del Ferrocarril, Manizales, Colombia
[d] CIT Santa Cruz (CONICET) – Facultad Regional Santa Cruz, Universidad Tecnológica Nacional, Río Gallegos, Argentina

ARTICLE INFO

Keywords:
Nanocomposites
Magnetic-nanoparticles
Graphene-oxide
SAXS
Magnetometry

ABSTRACT

A set of nanocomposites made of iron oxide nanoparticles covalently bonded to graphene oxide and reduced graphene oxide was successfully prepared. The synthesis was carried out in a precise step-by-step process in order to carefully control the nanocomposite formation. The nanocomposites were characterized by a range of techniques to verify the components arrangement according to the proposed strategy. Over the different samples, an in-depth study by Small Angle X-Ray Scattering (SAXS) and DC-Magnetometry was accomplished to analyze in detail the structure and properties of the systems. The results from this work indicate that the increase of the nanoparticle to graphene oxide ratio and the chemical reduction from graphene oxide to reduced graphene oxide modify the spatial distribution and the architecture of the nanoparticles over the sheets, leading to the formation of localized assemblies and bundle-like structures that have a significant impact on the macroscopicmagnetic behavior.

1. Introduction

In recent years, the development of novel complex materials produced by the combination of two or more nanostructures has become an area of extremely promising research. These new nanomaterials, or nanocomposites, benefit from the individual properties of each of the structure components, enabling the fabrication of systems with enhanced functionality and potential technological applications in various areas [1,2]. Graphene, a relatively novel carbon-based material, possesses extraordinary electrical, thermal, and mechanical properties [3], and has turned out to be an excellent candidate for constructing carbon-based nanocomposites when combined with other nanotechnology-related materials [4–6], such as metal nanoparticles (NPs) [7–10] and metal oxides NPs [11,12]. In particular, an oxygen-containing type of graphene known as graphene oxide (GO) has shown great potential for this kind of nanocomposites due to its low-cost bulk preparation and chemical versatility [13].

Many composites have been developed in the last years combining iron-based magnetic oxides and graphene oxide or reduced graphene oxide (rGO). These materials can be prepared by various synthetic routes. For instance, iron oxide NPs can be directly grown from the ionic iron precursors over the GO sheets by autoclave reaction [14], hydroxide co-precipitation [15–17], or thermal reaction in organic solvents [18,19]. Another approach implies coupling of pre-existent NPs through the formation of covalent bonds with the carboxylate groups present in the GO sheets [20–22]. The latter strategy disjoins the synthesis of the NPs from the formation of the composite, so the NPs quantity can be precisely controlled and the magnetic properties properly identified.

This type of iron oxide – graphene oxide nanocomposites showed very promising results when tested in various technological applications, such as magnetic-assisted absorption and separation [16,17,22], platforms for electrochemical sensing and catalysis [15,23] and as Magnetic Resonance Imaging contrast agent [18,24].

In this work, we expand on our previously reported results on the synthesis of composites formed by iron oxide NPs and GO/rGO [20]. The classical method for GO preparation, the so-called Hummers method [25], presents some drawbacks related to the GO structure

* Corresponding author.
E-mail addresses: ptancredi@fi.uba.ar (P. Tancredi), omoscosol@gmail.com, omoscoso@ifi.unicamp.br (O. Moscoso Londoño), privas@fi.uba.ar (P.C. Rivas Rojas), mknobel@ifi.unicamp.br (M. Knobel), lsocolovsky@fi.uba.ar, leandro.socolovsky@frsc.utn.edu.ar (L.M. Socolovsky).

https://doi.org/10.1016/j.materresbull.2018.08.003
Received 19 February 2018; Received in revised form 25 July 2018; Accepted 1 August 2018
Available online 02 August 2018
0025-5408/

homogeneity. Therefore, we decided to employ a newly developed synthesis route that improves the GO structure quality [26]. Two NPs-to-GO ratios were assayed, so four samples (two NPs@GO and two NPs@rGO) were produced and characterized. We focused our investigation on two physical characterization techniques: Small Angle X-Ray Scattering (SAXS) and Zero Field Cooling – Field Cooling Magnetometry. The information obtained from these techniques allows us to explore and understand the NPs assembly and distribution over the GO sheets and relate it to the macroscopic magnetic behavior of the nanocomposites.

2. Materials and methods

NPs@GO and NPs@rGO composites were prepared in a stepwise procedure inspired by previous published works [20,22].

2.1. Citric-coated iron oxide nanoparticles synthesis

The NPs were prepared by the co-precipitation of Fe^{3+}/Fe^{2+}. Briefly, 8.63 mmol of $FeCl_3$ and 4.31 mmol of $FeCl_2$ were dissolved in de-oxygenated water and co-precipitated with 10 mL of concentrated NH_4OH to form 1.00 g of Fe_3O_4. After 30 min, the NPs were magnetically decanted, washed with water and re-dispersed in 100 mL of a solution containing 4.00 g of citric acid and 2.25 g of NaOH (final pH = 7). The dispersion was heated to 90 °C and stirred for 3 h. The citric-coated NPs were centrifuged after precipitation with acetone, and finally re-dispersed in water to form a stable ferrofluid.

2.2. Silanization of NPs

A ligand exchange process was carried out to functionalize the citric-coated NPs with the amino-silane (3-Aminopropyl)triethoxysilane (APTES). An aliquot of the ferrofluid was diluted to a final volume of 200 mL and concentration of 1.25 mg/mL of iron oxide. 1 mL of APTES was added to the dilution and the mixture was refluxed under an Ar atmosphere. After 6 h of reaction, the solid was magnetically decanted, washed twice and redispersed in 50 mL of water.

2.3. Graphene oxide synthesis

GO was synthesized using a modified Hummers method [25,26]. According to Eigler et al. [26], the final GO structure can be optimized by carefully controlling the addition rate of the reagents and the temperature of the mixture during the procedure.

1.0 g of synthetic graphite (100 Mesh) and 0.5 g of sodium nitrate were added to 24 mL of concentrated H_2SO_4 and cooled to 0 °C. Then, 3.0 g of potassium permanganate was added over a period of 3 h while, keeping the temperature below 10 °C and stirred at 0 °C for additional 16 h. Afterwards, 20 mL of 10% H_2SO_4 and 60 mL of water were continuously added to the reaction mixture, carefully maintaining the system temperature below 10 °C. The reaction mixture was then poured into 500 mL of water at 0 °C, and 20 mL of 3% hydrogen peroxide was added dropwise until gas evolution was completed. The solid obtained (graphite oxide, GtO) was purified by repeated cycles of dispersion and centrifugation until the pH of the supernatant was neutral. Finally, GO was exfoliated from GtO in a slightly basic solution by mild sonication for 30 min and magnetic stirring for 16 h.

2.4. NPs@GO covalent bonding

The APTES@NPs dispersion was mixed with the exfoliated GO solution and water was added to a final volume of 200 mL. Two different ratios of NPs-to-GO were tested. Sample NPs@GO 1:2 was prepared with 125 mg of NPs and 250 mg of GO, while sample NPs@GO 2:1 with 250 mg of NPs and 125 mg of GO. The mixtures were heated to 80 °C and after 10 min 25 mg of 1-Ethyl-3-(3-dimethylaminopropyl) carbodiimide (EDC) and 25 mg of *N*-Hydroxysuccinimide (NHS) were added. The system was kept at reflux conditions for 24 h. Then, the NPs@GO composites were magnetically decanted, washed with H_2O and dried at room temperature inside a desiccator.

Finally, a fraction of NPs@GO 1:2 and 2:1 composites were treated with hydrazine to reduce GO to rGO [27]. We decided to use this reduction strategy instead of other existing alternatives, such as thermal [28,29] or photocatalytic reduction [30]. 0.2 g of NPs@GO was dispersed in 50 mL of H_2O. Then, 2 mL of hydrazine was added and the mixture was refluxed for 2 h The NPs@rGO composites were magnetically decanted, washed with H_2O and dried at room temperature inside a desiccator.

3. Sample characterization

X-ray diffraction (XRD) patterns were obtained on a standard Rigaku diffractometer with CuKα radiation. FTIR spectra were acquired at room temperature in the range 400–4000 cm^{-1} with a Shimadzu infrared spectrometer model IR-Prestige21, using the standard KBr method. Calorimetric analysis was carried out in a Thermo-Gravimetric Analyzer TGA-50 under static air atmosphere at a heating rate of 10 °C/min. Scanning electron microscopy (SEM) images were obtained with a Carl Zeiss Supra 40 field emission SEM microscope. Transmission electron microscopy (TEM) images were obtained in a JEOL JEM-2100F FEG-TEM microscope operated at 200 kV (C2Nano, LNNano, CNPEM, Campinas, Brazil). Samples were prepared by dripping 10 μL of dispersion in water onto a lacey carbon copper grid and vacuum-dried at room temperature. Hydrodynamic size by Dynamic light scattering (DLS) was measured using a Z Plus equipment by Brookhaven Instruments.

Small angle X-ray (SAXS) experiments were performed on SAXS-1 beamline at the Brazilian Synchrotron Light Laboratory (LNLS). The measurements were conducted at room temperature, using an X-ray wavelength of $\lambda = 1.822$ Å. Two sample distances to cover the rage of scattering vector $0.06 \leq q \leq 1.6\ nm^{-1}$. The acquisition time was 30 s. The scattering intensity was measured as function of the scattering vector defined, as $q = 4\pi \sin\theta/\lambda$, where θ is the scattering angle. Prior to data acquisition, powder samples of GO sheets, iron oxide nanoparticles and NPs@GO composites were diluted in water and sonicated for 1 h to then be injected into a 1-mm thick sample holder. The acquired SAXS data for NPs@GO composites was corrected according to the detector sensitivity, sample transmission, background scattering from GO sheets, water and sample holder mica disks. SAXS data was analyzed using a software from Paul Scherrer Institute [31].

The DC magnetization measurements were carried out using a Quantum Design SQUID magnetometer (MPMS *XL*). The zero-field cooling (ZFC) and field cooling (FC) magnetization curves were recorded following the standard protocols in a temperature range of 5 K–300 K, under an applied field of 20 Oe and a heating rate of 2 K/min. The isothermal magnetization curves were measured with a maximum applied field of 30 kOe.

4. Results and discussion

Fig. 1.a shows a TEM image of the NPs employed in the elaboration of the composite. The mean diameter of the synthesized particles is around 10.1 nm. The crystalline structure of the NPs obtained from XRD measurements of the dried powder confirms the formation of the magnetic *fcc* spinel-inverse iron oxide phase (Fe_3O_4 and/or γ-Fe_2O_3) as the only crystalline phase present in the system. The citric acid functionalization performed before the reaction with APTES is necessary to obtain a stable ferrofluid and avoid particle agglomeration as revealed by TEM images and DLS measurements. A well-dispersed ferrofluid as the starting material is essential to take advantage of the entire NPs surface and optimize the functionalization with the amino-silane molecules.

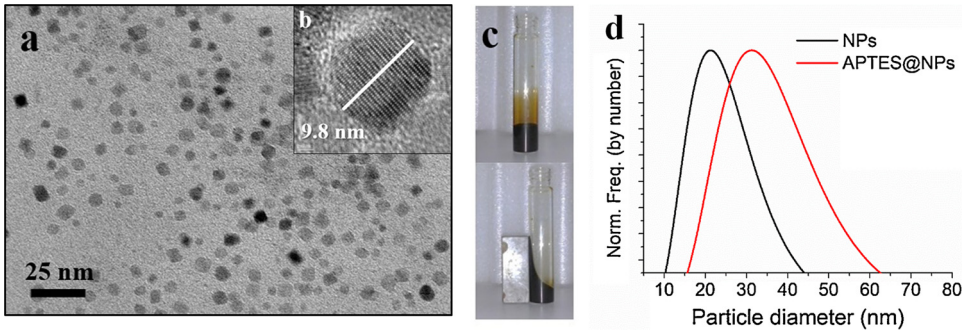

Fig. 1. a: TEM micrograph of citric-coated magnetic NPs. b: High-resolution image of a single NP. c: Ferrofluid before and after exposure to a magnetic field. d: Particle diameter distribution by DLS of citric-coated NPs and APTES@NPs.

After the amino-silane functionalization, the color of the ferrofluid changed from dark-brown to orange. The APTES modification was confirmed by the presence of the characteristic absorption bands of amine groups ($-NH_2$) and the stretching vibrations of Si—O bonds in the FTIR measurements. DLS measurements, presented in Fig. 1.d, exhibit an increase in the mean hydrodynamic size due to the SiO_2-shell and a small formation of clusters of tens of nanometers. Nevertheless, the obtained APTES@NPs dispersion remains stable for several days. The SiO_2-shell represents approximately 15% of the total mass of the APTES@NPs.

On the other hand, the synthetic graphite was successfully converted to GtO by the modified Hummers method, as confirmed by XRD. Fig. 2.a shows the XRD pattern of graphite and GtO. The characteristic interplanar spacing diffraction peak of graphite at 26° was shifted towards lower angles in the GtO sample. This result is attributed to the homogenous broadening of the graphene sheets interspacing caused by the oxidized groups. According to Bragg's law, the interplanar distance increased from 0.34 nm in graphite to 0.90 nm in GtO. The SEM image of the prepared sample (Fig. 2.b) shows a characteristic sheet-like structure. The graphene oxide layers are already exfoliated to a large extent, with a wrinkled structure that provides a large rough surface as scaffold for final exfoliation and further modification. Subsequently, the GtO can be easily dispersed in water to form a stable solution of GO sheets.

In the next step, the GO was mixed with the amine functionalized NPs and coupled via the EDC/NHS reaction. Two samples with different GO to NPs ratio were prepared, and the composites formation was analyzed by different characterization techniques. The temperature vs. weight-loss graphs obtained by TGA are shown in Fig. 3. In both NPs@GO 1:2 and NPs@GO 2:1 systems, an initial weight loss below 120 °C can be associated to the evaporation of adsorbed water. Then, a major drop at 200 °C denotes the starting point of the decomposition of labile oxygen-containing functional groups of GO present in the samples. The combustion of GO and subsequent mass loss continues with a

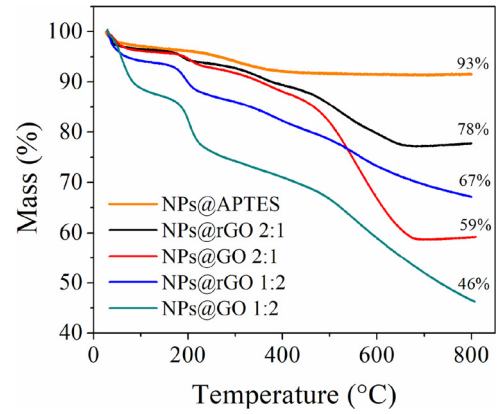

Fig. 3. TGA curves of APTES@NPs and the four composites. The percentage at the left indicate the final remaining mass.

homogeneous slope until 800 °C. The remaining mass at 800 °C can be related to the non-volatile iron oxide percentage in the composite, as GO is expected to be almost completely incinerated at this temperature. It is noteworthy that the mass ratio between the labile and stable phases obtained by TGA curves matches well with the precursor ratio employed in the elaboration of both composites.

For the NPs@rGO composites an important weight loss is also seen, but the shapes of the curves are clearly different to the ones of NPs@GO samples. The major drop in TGA curves for NPs@rGO occurs at 500 °C instead of 200 °C, suggesting a different pathway for the combustion reaction and some kind of modification in the carbon skeleton structure. In addition, the weight loss of both rGO composites is smaller than the respective GO composite. This could be related to the higher thermal stability of the samples due to the deletion of the carbon oxidized groups during the reduction reaction [32].

In the XRD patterns of the NPs@GO 1:2 and NPs@GO 2:1 systems

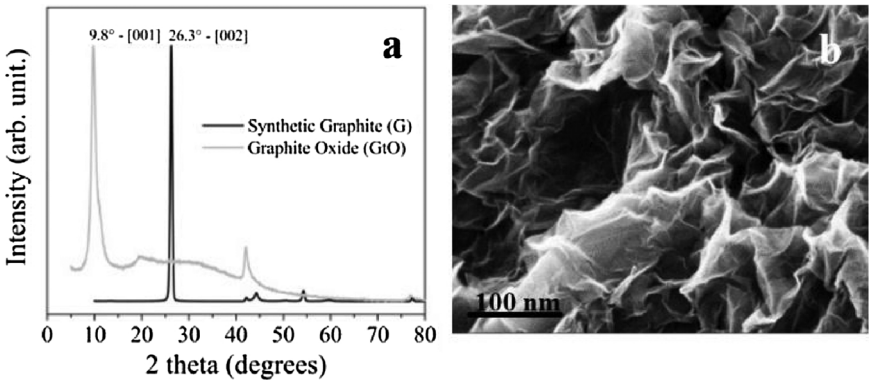

Fig. 2. a: XRD patterns of Synthetic Graphite and GtO. b: SEM image of GtO.

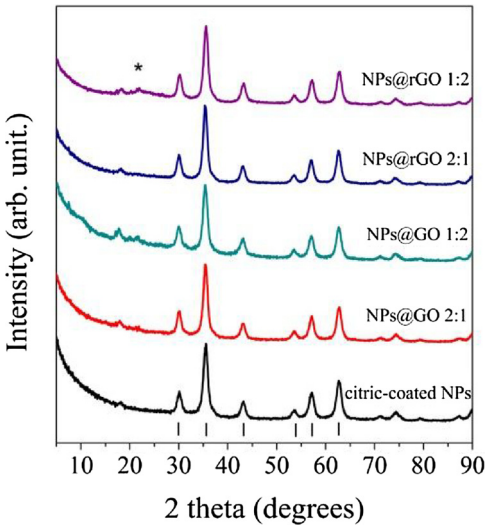

Fig. 4. XRD patterns of citric-coated NPs and the four composites. The diffraction peaks in all samples corresponds to spinel iron-oxide crystalline phase. * Points a peak at 24° that can be assigned to rGO stacking.

(Fig. 4), only the diffraction peaks of the iron oxide phase are revealed. Despite the TGA curves evidenced a significant amount of GO, the strong and clear diffraction peak at 9.3° associated to interplanar GO spacing does not appear in the composite diffraction pattern. This result suggests that the NPs acts as a spacer between the GO sheets and avoid homogeneous stacking after drying the dispersion. For the NPs@rGO 2:1 system the same result is obtained, while for NPs@rGO 1:2 a small peak at 24° can be associated with a small fraction of stacked rGO sheets.

SEM images of NPs@GO and NPs@rGO systems are presented in Fig. 5. In these micrographs, the functionalized NPs appear as bright dots and are well distributed along the GO and rGO sheets, with the formation of some localized clusters of particles. As suggested by the XRD patterns, the NPs act as a spacer by anchoring to both sides of the

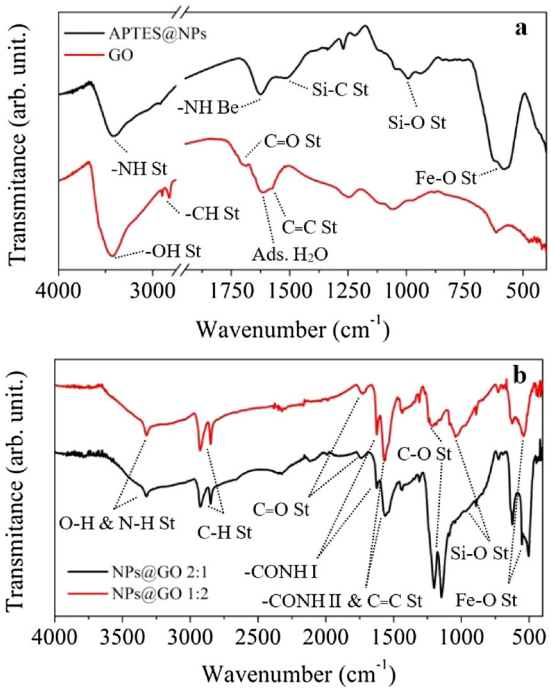

Fig. 6. FTIR spectra of a: APTES@NPs and GO, b: NPs@GO 1:2 and NPs@GO 2:1, with the corresponding band assignment for the observed peaks.

graphene sheets, in this case, the exposed and hidden sides of the superficial single layer.

Fig. 6 shows the FTIR data, with the detailed assignment of the absorption bands for each sample in the figure caption. The broad band at 3400 cm^{-1} in the GtO spectrum sums up the contribution of −OH groups bounded to the carbon skeleton and adsorbed H_2O molecules. Oxygen in the form of carbonyl groups is also revealed by the small shoulder at 1730 cm^{-1}. The narrow asymmetric peak at 1610 cm^{-1} can be a contribution from both C=C bonds (un-oxidized graphitic

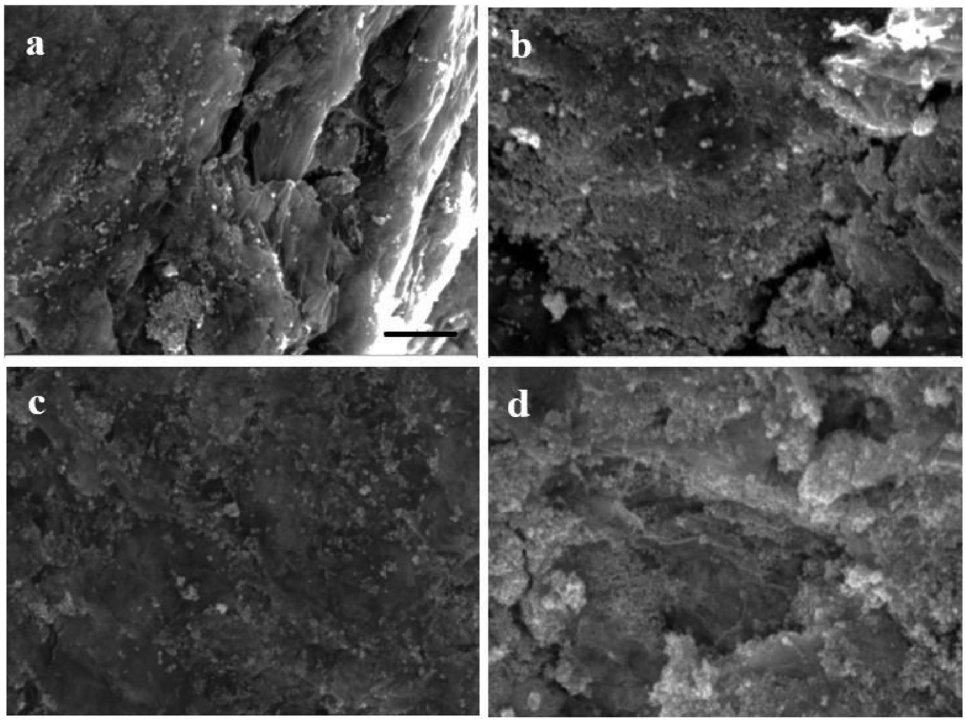

Fig. 5. SEM images of a: NPs@GO 1:2, b: NPs@GO 2:1, c: NPs@rGO 1:2, d: NPs@rGO 2:1. Scale bar = 200 nm.

domains) and adsorbed H_2O [26,33]. Bands below 1250 cm^{-1} may be associated to epoxy, hydroxyl groups and the skeletal C—C vibrational modes [26]. In summary, the GtO spectrum reveals all the expected bands for this material and is similar to the one obtained in Eigler et al. work, suggesting the good quality of the prepared GtO.

On the other hand, absorption bands from both components can be observed in the composites spectra. In addition, the formation of the amide bond can be inferred by the differences between the composites spectra and the APTES@NPs spectrum. At high wavenumbers, the characteristic —NH stretching band (3440 cm^{-1} in APTES@NPs) shifted towards lower energies (3320 cm^{-1}) because of the bond conjugation in the amide group. In addition, the wide —NH bending band at 1625 cm^{-1} observed in APTES@NPs vanishes in the two composites spectra and, in a similar location, a narrow peak at 1645 cm^{-1} is revealed and can be assigned to —CONH amide band I [22]. The other evidence of the bond formation, the —NH stretching band associated to the amide (band II), is overlapped with the C═C stretching band at 1550 cm^{-1} [22]. Like the TGA curves, the FTIR measurements also highlight the differences in NPs-to-GO ratio between the samples, with GO related bands (like —CH and C═C stretching) being more significant than Fe_3O_4 and SiO_2 related bands (like Si—O and Fe—O stretching) for composite NPs@GO 1:2 than for NPs@GO 2:1, and vice versa.

4.1. SAXS analysis

Small Angle X-ray Scattering (SAXS) was used as a structural characterization technique to analyze the global architecture of the composite. In a SAXS experiment, the whole sample volume is analyzed simultaneously, so it is possible to obtain more statistically accurate average structural values, as well as a defined idea of the architecture of the nanocomposite. Double-logarithmic plots of the experimental scattering curves are shown in Fig. 7.a and. b. There are a significant number of qualitative features visible in these curves. First, at the low-q region ($0.06\,nm^{-1} < q < 0.4\,nm^{-1}$) the scattered intensity of both systems displays a distinctive power law behavior instead of the typical Guinier behavior, commonly observed in a set of non-aggregated single nanoparticles [34]. The dependence, of $I(q)$ with $q^{-\alpha}$ (α being 2.5 and 2.6 for samples NPs@GO1:2 and 2:1, respectively) ratifies that the NPs form a compact collective structure randomly arranged over the GO sheets in each sample. Secondly, at high-q values, the two samples show essentially the same $I(q) \sim q^{-4}$ behavior, a distinctive feature of spherical nanoparticles with clearly defined borders [34]. Finally, at intermediate-q values, the lack of a well-developed oscillating behavior is an indicator of the polydisperse nature of the NPs and of possible interferences caused by proximate scattering objects.

Further information about the composites architectures was found by fitting the experimental SAXS data. The scattering intensity is modelled as a product of a form factor $P(q)$, which contain the characteristics of single NPs, such as dimensions and shape; and a structure factor $S(q)$, which captures the effect of the scattering interference between the neighboring NPs [35]. For this procedure, we assume a form factor for spherically symmetric particles smeared with a suitable size distribution, given by:

$$P(q, r, \Delta\eta) = \int_0^\infty K^2(q, r, \Delta\eta) f(r) dr \tag{1}$$

Here, $\Delta\eta$ is the scattering length density difference between nanoparticles and the surrounding medium, $f(r)$ the log-normal number distribution of NPs with median radius R_0, related to the mean diameter through:

$$\langle D_{SAXS} \rangle = 2R_0 e^{\sigma^2/2}. \tag{2}$$

The function that takes into account the NPs spherical shape is:

$$K^2(q, r, \Delta\eta) = \frac{4}{3}\pi r^3 \Delta\eta \left[3\frac{\sin(qr) - qr\cos(qr)}{(qr)^3} \right]. \tag{3}$$

As mentioned above, the functional dependence of $I(q)$ with $q^{-\alpha}$ and the obtained α values at low-q values suggest the formation of NPs aggregates with a fractal structure, according to the fixed assembly of NPs over the GO sheets. Then, a structure factor $S(q)$ derived from the fractal aggregate model was chosen. Such model, described by Teixeira and Chem [36,37], establishes that the power law form ($q^{-\alpha}$, being α the fractal dimension) of the scattering function is limited by a finite cluster size ξ appearing as a cut-off function $h(r, \xi)$. Generally speaking, the structure factor $S(q)$ that describes a system composed by fractal aggregates can be written as:

$$S(q) = 1 + \frac{\alpha}{R_0^\alpha} \int_0^\infty r^{(\alpha-3)} h(r, \xi) \frac{\sin(qr)}{qr} dr \tag{4}$$

There are several cut-off functions that have been applied on different nanostructured systems [31], some of them, discussed and compared by Sorensen et al. [38]. However, the exponential cut-off function:

$$h_{\exp}(r, \xi) = e^{-\frac{r}{\xi}} \tag{5}$$

has been successfully applied in similar nanocomposites in order to extract important structural parameters [39]. Then, using $h_{exp}(r, \xi)$, the Eq. (4) can be analytically solved to obtain [31]:

$$S(q) = 1 + \frac{\alpha\Gamma(\alpha-1)}{(qR_0)^\alpha} \frac{\sin[(\alpha-1)\tan^{-1}(q\xi)]}{\left[1 + \frac{1}{(q\xi)^2}\right]^{\frac{\alpha-1}{2}}}, \tag{6}$$

being $\Gamma(x)$ the gamma function. By using the proposed model, the experimental SAXS intensities of samples NPs@GO1:2 and 2:1 were successfully fitted (continuous lines at Fig. 7.a and. b). This means that only the mass fractal contribution was needed to consider the interparticle interference into the cluster and thus, to fit the entire curves. Relevant associated parameters are listed in Table 1. Fig. 7.c reports the structure factor evolution with q. In both samples, this $S(q)$ factor clearly displays a power law dependence on $q^{-\alpha}$ in the lower-q range.

The obtained primary nanoparticle diameter ($\langle D \rangle_{SAXS}$) and the SAXS log-normal size distributions suitably corresponds to the particle size distributions shown in the histograms (Fig. 7.d). The most significant difference is the width of the size distributions. The SAXS size distribution is broader than the calculated from the TEM histograms, but narrower to the hydrodynamic size distribution obtained by DLS measurements. This effect can have several origins, such as, for example, an irregular distribution of silica coatings generated during the functionalization procedure or the presence of small close-packed aggregates of NPs in the dispersion before the conjugation reaction. Furthermore, it must be considered that TEM images were conducted on an ultra-diluted NPs dispersion, while SAXS experiments were carried out on samples where the NPs are arranged on bundles (areas with higher concentration) over the GO sheets, which leads to an overestimation of the polydispersity due to increasing particle interactions [40]. The estimated fractal dimensions and the finite cluster sizes (being α 2.5 and 2.7; and ξ 39.2 nm and 107.8 nm for samples NPs@GO 1:2 and 2:1, respectively) indicate that the NPs on the GO sheets are prone to form bundle-like structures with a three-dimensional architecture [39], being denser and larger on sample NPs@GO 2:1, accordingly the larger NPs concentration. In summary, the SAXS results evidence the strong dependency of the NPs architecture with the mass ratio between them and the GO sheets.

4.2. Magnetization results

Previously, the SAXS data analysis indicated that the nanoparticle arrangements over the GO sheets differ between the two studied

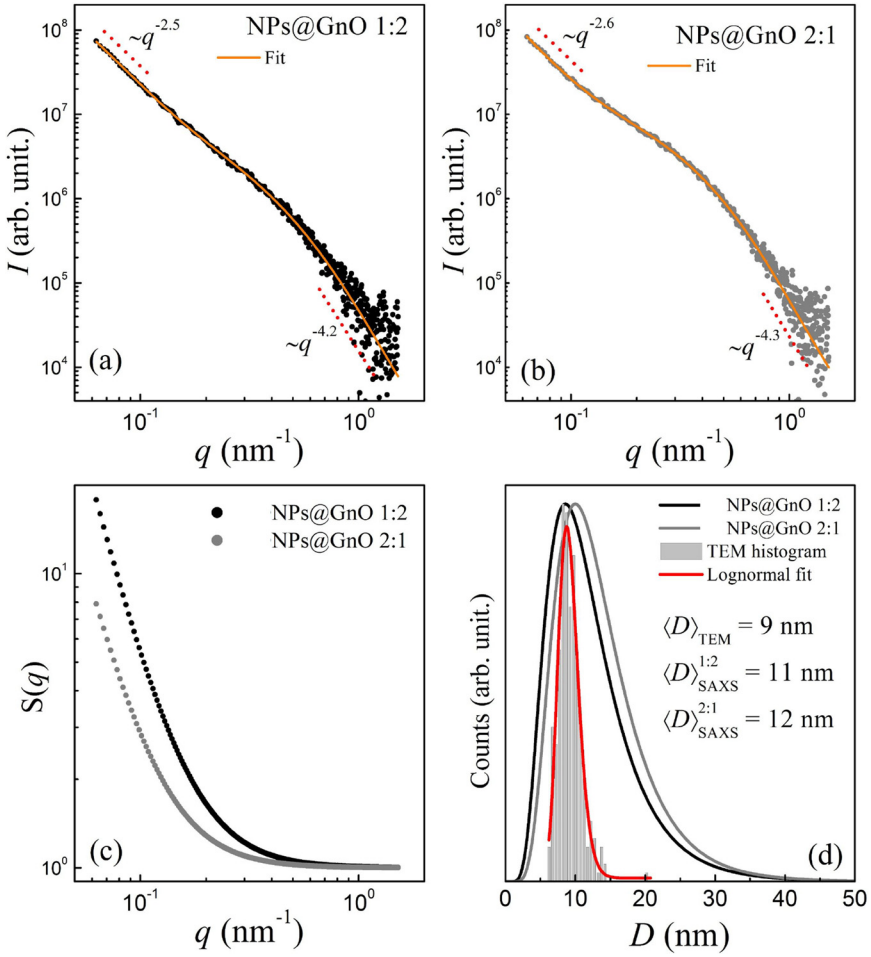

Fig. 7. SAXS profiles of a: NPs@GO 1:2, b: NPs@GO 2:1. Fitted curves are presented as a continuous line. c: log-log plot of the structure factor function S(q). d: TEM NPs diameter histogram (gray bars) and log-normal fitted curve (red line). SAXS log-normal size distribution of NPs from NPs@GO 1:2 (black line) and NPs@GO 2:1 (grey line). (For interpretation of the references to colour in this figure legend, the reader is referred to the web version of this article.)

Table 1
SAXS fitted parameters. Mean primary nanoparticle diameter ($\langle D\rangle_{SAXS}$), log-normal standard deviation (σ), fractal dimension (α) and cluster size (ξ).

Sample	$\langle D\rangle_{SAXS}$ (nm)	σ	α	ξ (nm)
NPs@GO 1:2	11	0.47	2.5	39.2
NPs@GO 2:1	12	0.45	2.7	107.8

samples, i.e., despite that the formation of some aggregates and bundles-like structures were detected in both composites, larger and denser ones were found in sample NPs@GO 2:1. In order to evaluate the NPs assembly effect on the magnetic properties, the temperature and magnetic field dependence of the magnetization were measured. Fig. 8 compares the zero field cooling (ZFC) and field cooling (FC) magnetization curves of the NPs@GO and NPs@rGO samples. The four measurements exhibit the typical characteristics of polydisperse weakly interacting magnetic NPs systems [41], with a clear and broad maximum for the ZFC curve (peak temperature, T_M). The temperatures of these peaks are 147 K for NPs@GO 1:2, 183 K for NPs@GO 2:1, 178 K NPs@rGO 1:2 and 211 K for NPs@rGO 2:1.

For ideal strongly diluted systems, both T_M and the general shape of the ZFC-FC curves are intrinsically defined by the NPs characteristics (shape, size, anisotropy, etc.) [42]. However, the shape of the ZFC curves of the samples exhibit different broadening and small shifts between the maximum values, even though the same NPs precursor was employed for all the samples. This variation can be ascribed to nanoparticle magnetic interactions of dipolar origin. The dipolar interactions can indeed modify the magnetic behavior of nanoparticle systems, i.e., by shifting T_M towards higher temperatures or by flattening the FC curve for T < T_M [40,42]. The decrease in the spatial separation of the NPs by increasing their concentration and the formation of localized clusters usually leads to higher dipolar interactions. This may be the case of the four samples under study. In a first comparison between the NPs@GO systems, T_M occurs at a higher temperature and the FC curve is flattened in the sample NPs@GO 2:1, the composite with a higher NPs concentration and cluster density. In addition, the T_M values of the NPS@rGO systems are above than the respective T_M of the pre-treated sample. These changes in the ZFC-FC curves suggest that the chemical reduction process modifies the architecture of the NPs assemblies over the carbon sheets, decreasing the NPs interparticle spacing and leading to the formation of some localized clusters.

Based on the information from SEM, SAXS and ZFC-FC analysis, the studied magnetic composites can be considered as weakly interacting systems with a moderate NPs size dispersion. This fact allows us to consider the peak temperature (T_M) as a good approximation to the point in which the system evolves from the blocked to the superparamagnetic regime, i.e. close to the so-called blocking temperature (T_B). With the blocking temperature value, it is possible to estimate an effective anisotropy constant, K_{eff}, by means of the functional ratio, $K_{eff} = 25k_BT_B/V$, where k_B is the Boltzmann constant and V the mean nanoparticle volume. The calculated anisotropies are listed in Table 2. As expected, larger values of K_{eff} were found in samples with higher T_M,

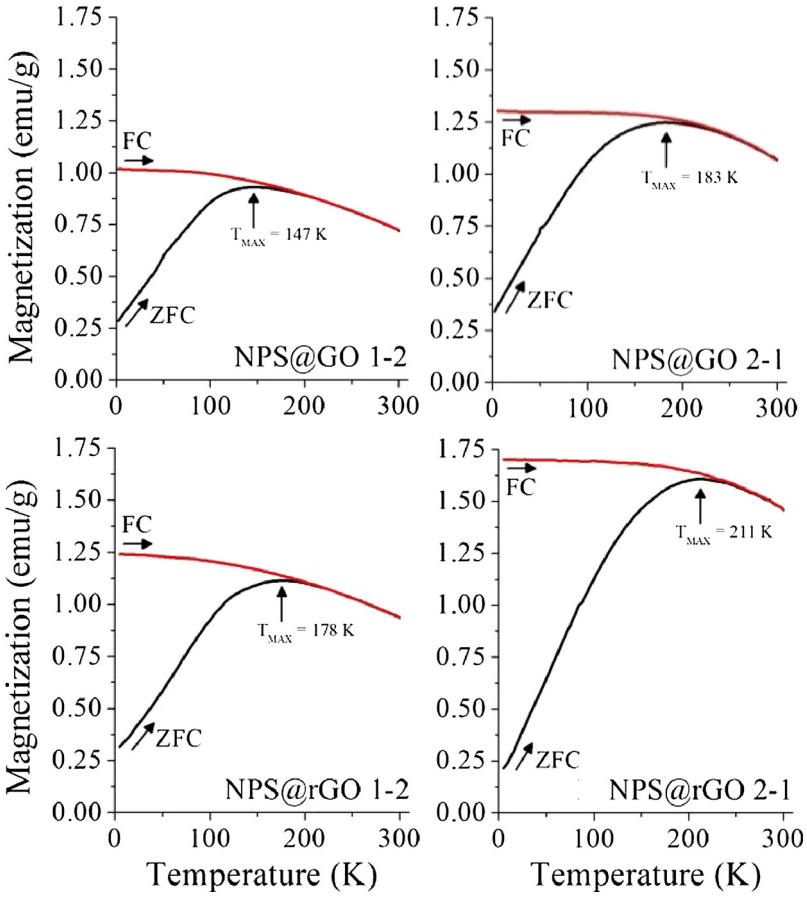

Fig. 8. Zero Field Cooled (ZFC) and Field Cooled (FC) curves of the four studied composites. External magnetic field = 20 Oe. Arrows shows the peak temperature of the ZFC curves (T_{MAX}).

Table 2
Magnetic properties: M_S, Saturation magnetization per gram of composite; N, number of magnetic nanoparticles per unit volume in a superparamagnetic regime; $\langle\mu\rangle$, mean magnetic moment, determined from $\langle\mu\rangle = x_0 e^{\sigma^2/2}$, were x_0 is the median of the distribution and σ is the standard deviation.

Sample	T_B[a]	K_{eff}[b] (10^6 erg/cm^3)	M_S (emu/g)	% of Fe_3O_4	N[c] (10^{16} cm^{-3})	$\langle\mu\rangle$[c] (10^3 μ_B)	σ[c]
NPs@GO 1:2	147	1.3	32	42	1.3	8.2	1.07
NPs@GO 2:1	183	1.6	48	63	1.4	8.1	0.98
NPs@rGO 1:2	178	1.6	33	43	1.2	9.1	1.10
NPs@rGO 2:1	211	1.9	51	67	1.2	9.0	1.08

[a] Maximum of the ZFC curve.
[b] Calculated from $K_{eff} = 25 k_B T_B / V$.
[c] From M vs. H curves fit.

a behavior that may be related to the increase of the energy barrier caused by the dipolar interactions ($E_B \propto K_{eff}V$) or to the existence of collective effects [43].

Fig. 9 shows the Magnetization vs. Field (M vs. H) curves at room temperature (T = 300 K) of both NPs@GO and NPs@rGO systems. The experimental curves do not have remanent magnetization nor coercive field, confirming that the systems are superparamagnetic and the NPs are superparamagnetic at room temperature. Taking into account that the contribution of GO and rGO to the magnetization response is practically negligible, the saturation magnetization (M_s) values and a comparison with M_s of pure magnetite NPs (78 emu/g) can give us an approximate idea of the Fe_3O_4 amount in each sample. The M_s values and the Fe_3O_4 fraction according to this analysis are given in Table 2.

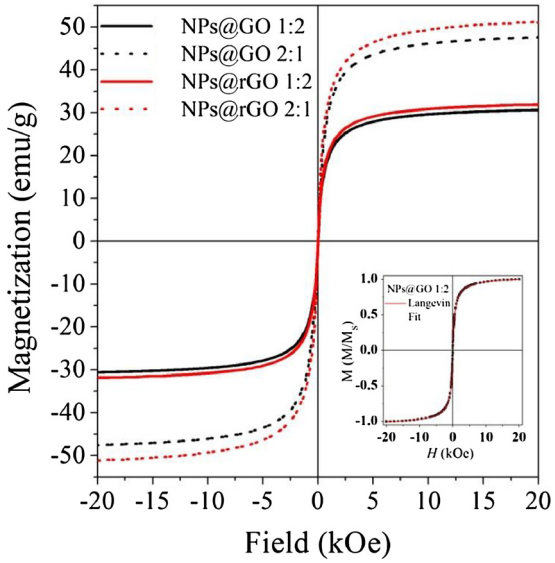

Fig. 9. Magnetization vs. Applied magnetic field curve at T = 300 K of the four composites. Inset: Reduced magnetization for sample NPs@GO 1:2 (black points) and Langevin equation fit (red line). (For interpretation of the references to colour in this figure legend, the reader is referred to the web version of this article.)

For NPs@GO composites, the calculated percentages of iron oxide are in good agreement with the remaining mass observed in TGA, as the GO and the APTES alkyl chains were expected to be complete incinerated in those runs. The small differences in favor of the TGA measurement

percentage can be attributed to the remaining SiO_2 shell. On the other hand, a small increase of M_s after the reduction process is observed and can be associated to some minor changes in composite proportions. Due to the removal of oxygen atoms of carbon oxidized groups during the reaction with hydrazine, rGO sheets are slightly lighter than GO sheets, thus modifying the percentage of the magnetic phase in the final product. Also, for these latter cases, the calculated percentage of iron oxide differs with the remaining mass value observed in TGA, suggesting that the rGO sheets are not completely incinerated despite the air atmosphere employed in the runs. The estimated percentage of rGO according to TGA and magnetic measurements is 52% for NPs@rGO 1:2 and 27% for NPs@rGO 2:1.

Above the irreversibility temperature the magnetization dynamics of a set of weakly interacting magnetic NPs are well described by the superparamagnetic theory [44], and the magnetization curves can be modeled by the Langevin function, $L(x)$. We employ this function to fit the data at T = 300 K and thus extract important parameters such as the mean magnetic moment ($\langle\mu\rangle$), the number of magnetic NPs in a superparamagnetic regime (N), among others. To describe the real magnetization data, $L(x)$ was weighted by a suitable log-normal type moment distribution function, $f(\mu)$, to take into account the dispersion of the nanoparticles. Thus, the fitted equation is:

$$M(H) = N\int_0^\infty \mu L\left(\frac{\mu H}{k_B T}\right) f(\mu)d\mu + C \tag{7}$$

where C is a parameter that accounts for paramagnetic contribution at high magnetic fields. The experimental magnetization curves were well fitted by Eq. (6) (*inset* at Fig. 9), and the inferred parameters are summarized in Table 2. The values are within the expected range for superparamagnetic systems composed by magnetite nanoparticles, *i.e.*, $\sim 10^3\ \mu_B$ for the mean magnetic moment and $\sim 10^{16}\,\mathrm{cm}^{-3}$ for the number of magnetic nanoparticles in superparamagnetic regime per unit volume. The small differences could be related to modifications of the dipolar energy due to minor changes in the magnetic dipolar interactions.

5. Conclusions

In summary, we managed to successfully synthesize a set of nanocomposites based on Fe_3O_4 nanoparticles covalently bonded to graphene oxide and reduced graphene oxide sheets. We accomplished a complete characterization of the composites in order to study the final structure of the samples and prove the link between the starting materials. The employed synthesis strategy allowed us to control the NPs-to-GO ratio in the composite in a precise manner. Moreover, we employed some novel characterization techniques on these magnetic NPs@GO and NPs@rGO composites to achieve a better understanding of their assembly process and architecture. We found that an increase in the NPs-to-GO ratio and the reduction from GO to rGO modifies the spatial distribution of the NPs over the sheets, leading to the formation of localized assemblies and bundle-like structures that affects the magnetic behavior.

Conflicts of interest

There are no conflicts of interest to declare.

Acknowledgements

This work was partially supported by Consejo Nacional de Investigaciones Científicas y Tecnológicas (CONICET) and Fundação de Amparo à Pesquisa do Estado de São Paulo (FAPESP, grant 2014/26672-8). We acknowledge LNNano and LNLS (CNPEM-Brazil), for the use of HR-TEM and SAXS line, respectively. We are grateful to Dr. Edilso Reguera and Dra. Donaji Velazco from REMILAB – CICATA (Unidad Legaria, IPN, México) for their multiple helps.

References

[1] J.B. Haun, T.J. Yoon, H. Lee, R. Weissleder, Magnetic nanoparticle biosensors, Wiley Interdiscip. Rev. Nanomed. Nanobiotechnol. 2 (2010) 291–304.
[2] M. Zhi, C. Xiang, J. Li, M. Li, N. Wu, Nanostructured carbon-metal oxide composite electrodes for supercapacitors: a review, Nanoscale 5 (2013) 72–88.
[3] S. Park, R.S. Ruoff, Chemical methods for the production of graphenes, Nat. Nanotechnol. 4 (2009) 217–224.
[4] S. Stankovich, D.A. Dikin, G.H. Dommett, K.M. Kohlhaas, E.J. Zimney, E.A. Stach, R.D. Piner, S.T. Nguyen, R.S. Ruoff, Graphene-based composite materials, Nature 442 (2006) 282–286.
[5] H. Kim, A.A. Abdala, C.W. Macosko, Graphene/polymer nanocomposites, Macromolecules 43 (2010) 6515–6530.
[6] O.C. Compton, S.T. Nguyen, Graphene oxide, highly reduced graphene oxide, and graphene: versatile building blocks for carbon-based materials, Small 6 (2010) 711–723.
[7] C. Xu, X. Wang, J. Zhu, Graphene-metal particle nanocomposites, J. Phys. Chem. C 112 (2008) 19841–19845.
[8] Y.G. Zhou, J.J. Chen, F.B. Wang, Z.H. Sheng, X.H. Xia, A facile approach to the synthesis of highly electroactive Pt nanoparticles on graphene as an anode catalyst for direct methanol fuel cells, Chem. Commun. 46 (2010) 5951–5953.
[9] T.A. Pham, N.A. Kumar, Y.T. Jeong, Covalent functionalization of graphene oxide with polyglycerol and their use as templates for anchoring magnetic nanoparticles, Synth. Met. 160 (2010) 2028–2036.
[10] S. Yang, J. Dong, Z. Yao, C. Shen, X. Shi, Y. Tian, S. Lin, X. Zhang, One-pot synthesis of graphene-supported monodisperse Pd nanoparticles as catalyst for formic acid electro-oxidation, Sci. Rep. 4 (2014) 4501.
[11] H. Wang, L.-F. Cui, Y. Yang, H.S. Casalongue, J.T. Robinson, Y. Liang, Y. Cui, A.H. Dai, Mn_3O_4-graphene hybrid as a high-capacity anode material for lithium ion, J. Am. Chem. Soc. (2010) 13978–13980.
[12] N. Li, M. Zheng, X. Chang, G. Ji, H. Lu, L. Xue, L. Pan, J. Cao, Preparation of magnetic CoFe2O4-functionalized graphene sheets via a facile hydrothermal method and their adsorption properties, J. Solid State Chem. 184 (2011) 953–958.
[13] D. Chen, H. Feng, J. Li, Graphene oxide: preparation, functionalization, and electrochemical applications, Chem. Rev. 112 (2012) 6027–6053.
[14] D. Zhou, T.-L. Zhang, B.-H. Han, One-step solvothermal synthesis of an iron oxide–graphene magnetic hybrid material with high porosity, Microporous Mesoporous Mater. 165 (2013) 234–239.
[15] H. Teymourian, A. Salimi, S. Khezrian, Fe3O4 magnetic nanoparticles/reduced graphene oxide nanosheets as a novel electrochemical and bioeletrochemical sensing platform, Biosens. Bioelectron. 49 (2013) 1–8.
[16] Y. Yao, S. Miao, S. Liu, L.P. Ma, H. Sun, S. Wang, Synthesis, characterization, and adsorption properties of magnetic Fe3O4@graphene nanocomposite, Chem. Eng. J. 184 (2012) 326–332.
[17] V. Chandra, J. Park, Y. Chun, J.W. Lee, I.-C. Hwang, K.S. Kim, Water-dispersible magnetite-reduced graphene oxide composites for arsenic removal, ACS Nano 4 (2010) 3979–3986.
[18] H. He, C. Gao, Supraparamagnetic, conductive, and processable multifunctional graphene nanosheets coated with high-density Fe3O4 nanoparticles, ACS Appl. Mater. Interfaces 2 (2010) 3201–3210.
[19] J. Shen, Y. Hu, M. Shi, N. Li, H. Ma, M. Ye, One step synthesis of graphene oxide-magnetic nanoparticle composite, J. Phys. Chem. C 114 (2010) 1498–1503.
[20] C. Cosio-Castañeda, R. Martínez-García, L.M. Socolovsky, Synthesis of silanized maghemite nanoparticles onto reduced graphene sheets composites, Solid State Sci. 30 (2014) 17–20.
[21] W. Chen, P. Yi, Y. Zhang, L. Zhang, Z. Deng, Z. Zhang, Composites of aminodextran-coated Fe3O4 nanoparticles and graphene oxide for cellular magnetic resonance imaging, ACS Appl. Mater. Interfaces 3 (2011) 4085–4091.
[22] F. He, J. Fan, D. Ma, L. Zhang, C. Leung, H.L. Chan, The attachment of Fe3O4 nanoparticles to graphene oxide by covalent bonding, Carbon 48 (2010) 3139–3144.
[23] S. Zhu, J. Guo, J. Dong, Z. Cui, T. Lu, C. Zhu, D. Zhang, J. Ma, Sonochemical fabrication of Fe3O4 nanoparticles on reduced graphene oxide for biosensors, Ultrason. Sonochem. 20 (2013) 872–880.
[24] H.P. Cong, J.J. He, Y. Lu, S.H. Yu, Water-soluble magnetic-functionalized reduced graphene oxide sheets: in situ synthesis and magnetic resonance imaging applications, Small 6 (2010) 169–173.
[25] W.S. Hummers, R.E. Offerman, Preparation of graphitic oxide, J. Am. Chem. Soc. 80 (1958) 1339.
[26] S. Eigler, M. Enzelberger-Heim, S. Grimm, P. Hofmann, W. Kroener, A. Geworski, C. Dotzer, M. Rockert, J. Xiao, C. Papp, O. Lytken, H.P. Steinruck, P. Muller, A. Hirsch, Wet chemical synthesis of graphene, Adv. Mater. 25 (2013) 3583–3587.
[27] S. Pei, H.-M. Cheng, The reduction of graphene oxide, Carbon 50 (2012) 3210–3228.
[28] X. Gao, J. Jang, S. Nagase, Hydrazine and thermal reduction of graphene oxide: reaction mechanisms, product structures, and reaction design, J. Phys. Chem. C 114 (2010) 832–842.
[29] Z. Wei, D. Wang, S. Kim, S.-Y. Kim, Y. Hu, M.K. Yakes, A.R. Laracuente, Z. Dai, S.R. Marder, C. Berger, W.P. King, W.A. de Heer, P.E. Sheehan, E. Riedo, Nanoscale tunable reduction of graphene oxide for graphene electronics, Science 328 (2010) 1373–1376.
[30] G. Williams, B. Seger, P.V. Kamat, TiO2-graphene nanocomposites. UV-assisted photocatalytic reduction of graphene oxide, ACS Nano 2 (2008) 1487–1491.

[31] J. Kohlbrecher, A Program for Fitting Simple Structural Models to Small Angle Scattering Data, Paul Scherrer Institute Laboratory for Neutron Scattering, 2014.
[32] P. Cui, J. Lee, E. Hwang, H. Lee, One-pot reduction of graphene oxide at subzero temperatures, Chem. Commun. 47 (2011) 12370–12372.
[33] N. Wu, X. She, D. Yang, X. Wu, F. Su, Y. Chen, Synthesis of network reduced graphene oxide in polystyrene matrix by a two-step reduction method for superior conductivity of the composite, J. Mater. Chem. 22 (2012) 17254.
[34] C. Meiorin, D. Muraca, K.R. Pirota, M.I. Aranguren, M.A. Mosiewicki, Nanocomposites with superparamagnetic behavior based on a vegetable oil and magnetite nanoparticles, Eur. Polym. J. 53 (2014) 90–99.
[35] O. Glatter, O. Kratky, Small Angle X-Ray Scattering, Academic Press, New York, United States, 1982.
[36] J. Teixeira, Small-angle scattering by fractal systems, J. Appl. Crystallogr. 21 (1988) 781–785.
[37] S.H. Chen, J. Teixeira, Structure and fractal dimension of protein-detergent complexes, Phys. Rev. Lett. 57 (1986) 2583–2586.
[38] C.M. Sorensen, J. Cai, N. Lu, Test of static structure factors for describing light scattering from fractal soot aggregates, Langmuir 8 (1992) 2064–2069.
[39] J.M. Orozco-Henao, D.F. Coral, D. Muraca, O. Moscoso-Londoño, P. Mendoza Zélis, M.B. Fernandez van Raap, S.K. Sharma, K.R. Pirota, M. Knobel, Effects of nanostructure and dipolar interactions on magnetohyperthermia in iron oxide nanoparticles, J. Phys. Chem. C 120 (2016) 12796–12809.
[40] V. Goertz, N. Dingenouts, H. Nirschl, Comparison of nanometric particle size distributions as determined by SAXS, TEM and analytical ultracentrifuge, Part. Part. Syst. Charact. 26 (2009) 17–24.
[41] M. Knobel, W.C. Nunes, L.M. Socolovsky, E.D. Biasi, J.M. Vargas, J.C. Denardin, Superparamagnetism and other magnetic features in granular materials: a review on ideal and real systems, J. Nanosci. Nanotechnol. 8 (2008) 2836–2857.
[42] L.M. Socolovsky, O. Moscoso-Londoño, Consequences of magnetic interactions phenomena in granular systems, in: S.K. Sharma (Ed.), Complex Magnetic Nanostructures - Synthesis, Assembly and Applications, Springer, Rio de Janeiro, 2017.
[43] P. Allia, M. Coisson, P. Tiberto, F. Vinai, M. Knobel, M.A. Novak, W.C. Nunes, Granular Cu-Co alloys as interacting superparamagnets, Phys. Rev. B 64 (2001) 144420.
[44] C.P. Bean, J.D. Livingston, Superparamagnetism, J. Appl. Phys. 30 (1959) S120–S129.